Numerical simulations of experimental fluid-induced vibrations of cylinders in cross-flow

Daniele Vivaldi, Guillaume Ricciardi

NUMERICAL SIMULATIONS OF EXPERIMENTAL FLUID-INDUCED VIBRATIONS OF CYLINDERS IN CROSS-FLOW

Daniele Vivaldi
Institut de Radioprotection et de Sûreté Nucléaire (IRSN)
Cadarache, St Paul-lez-Durance, BP3, 13115, France

Guillaume Ricciardi
Commissariat à l'Energies Atomique et aux Energies Alternatives
CEA/DES/IRESNE, Dep. of Nuclear Technology
Cadarache F-13108 Saint-Paul-Lez-Durance

ABSTRACT

This paper presents fluid-structure interaction (FSI) simulations of a published experimental campaign dedicated to the study of fluid-induced vibrations on cylinders. The experimental configuration consists in two in-line cylinders subjected to water cross-flow. This experimental campaign is relevant for numerical FSI validation purposes, since it accesses both fluid and structure measurements. This paper presents the numerical simulations of one of the different water flow rates tested experimentally. The FSI simulations are run with the CFD code code_Saturne: a two-way coupling between the fluid and the structure is realized thanks to the implementation of an Euler-Bernoulli finite element beam model inside code_Saturne. This paper describes the FSI approach and presents its application to the experimental configuration considered. Numerical results are compared to the experimental ones, in terms of velocity fluctuations behind the cylinders and vibrations of the cylinders. Fluid simulations are realized retaining both a URANS approach and the Scale Adaptive Simulation (SAS) hybrid URANS/LES approach.

1. INTRODUCTION

Fluid-structure interaction (FSI) of slender structures is a concern in nuclear power plants (NPPs). Two main examples are the vibrations of fuel rods and fuel assemblies due to the single phase water flow inside the reactor pressure vessel, and the vibrations of U-tube steam generator (SG) tubes due to the two-phase steam-water flow. Thanks to the increasing computational performances, the numerical simulation of FSI phenomena has become more and more feasible in the recent years. Several numerical simulation results of NPP relevant FSI phenomena have been published by several authors. From the numerical point of view, the main challenge of performing FSI simulations is their high CPU requirements: this is due to the coupled solution of the fluid and the solid fields, which, generally speaking, requires a 3D Computational Fluid Dynamics (CFD) solution and a 3D Finite Element Model (FEM) solution, together with a large amount of data sharing between the two. Coupled fluid-structure simulations of flow-induced vibrations (FIV) of fuel rods with spacer grids employing CFD and FEM have been presented by, for example, Liu et al (2017). De Santis, Kottapalli and Shams (2018), De Santis and Shams (2019) and Brockmeyer et al (2018) presented FSI simulations of FIV in wire-wrapped fuel pin bundles, also using CFD and FEM. Reduced-order models can be a powerful option, when physically consistent, in the frame of FSI simulations, since they allow to decrease the computational time. Christon et al (2016), for example, calculated fuel rod vibration response under axial flow, employing CFD and a solid model based on the Euler-Bernoulli beam theory. Reduced order models applied to slender structures, such as rods and tubes, have been published recently by, for example, Baraglia, Benguigui and Denefle (2021) and Papukchiev (2019). Shinde et al (2014) and Berland, Deri and Adobes (2016) simulated FSI of tube bundles in cross-flow (configuration representative of the U-bend region of U-tube SGs): thanks to the experimental rigid translational motion (i.e., with no deformation), the authors could retain a 1 degree of freedom mass-damp-stiffness approach to calculate the tube motion.

From the FSI result validation point of view, the main current difficulty lies in the fact that most of the published numerical studies (such as the ones mentioned above) rely only on the structure vibration experimental measurements, and suffer from a lack of experimental knowledge of the fluid flow (local velocity measurements). Numerical results are therefore compared in terms of vibration response, with no insight on the consistency of the flow behavior prediction:

this prevents from a comprehensive validation of the numerical results.
Experimental campaigns accessing both structure and fluid behavior are mandatory in order to validate and assess strengths and weaknesses of a specific FSI numerical model. For this purpose, this paper considers the experimental campaign recently realized by Bolshukhin et al (2021), who published velocity measurements of a water cross-flow behind two in-line cylinders, together with the cylinder fluid-induced vibration measurements. Numerical FSI simulations of this experimental campaign were performed, and numerical results were compared to the experimental ones in terms of both fluid velocities and structure vibrations. The coupled fluid-structure simulations employ CFD for the fluid field, whereas the cylinders are simulated through a reduced-order model, based on the Euler-Bernoulli beam theory.

2. EXPERIMENTAL CONFIGURATION

The experimental campaign considered is the one realized by Bolshukhin et al (2021). The configuration consists of two in-line cylinders in water cross-flow. The goal of this configuration is the study of vibrations induced by vortex shedding behind the cylinders.
The cylinders have a cantilever attachement on one end, and a free end inside the channel. The length of the cylinders is 198mm, the test section height is 200mm, which means that only 2 millimeters separate the cylinder free end from the test section top wall. The cylinder diameter is 7.0mm. They are made of metal thin-walled tube, the wall thickness is 0.3mm. The distance between the two cylinders is 45mm. A picture of the test section and the dimensions of the channel are provided in Fig. 1: water flows from left to right, as indicated by the arrow.
The material of the cylinders is stainless steel. Accelerometers are mounted inside the cylinders via a brass rod. Since the brass rods employed for the two cylinders are not identical, the natural frequency (f_n) of the cylinders is not the same: f_n of the first cylinder is 98Hz in water, f_n of the second cylinder is 90Hz in water.
LDV and PIV are employed to measure velocity profiles and velocity fluctuations behind the cylinders (see Fig. 2). The velocity spectra behind the cylinders can therefore be calculated, in order to obtain the frequency content. Instantaneous static pressure is measured in four locations on the test section wall, as shown in Fig. 2.
Regarding the cylinder vibrations, the acceleration is monitored for each cylinder: the acceleration spectra

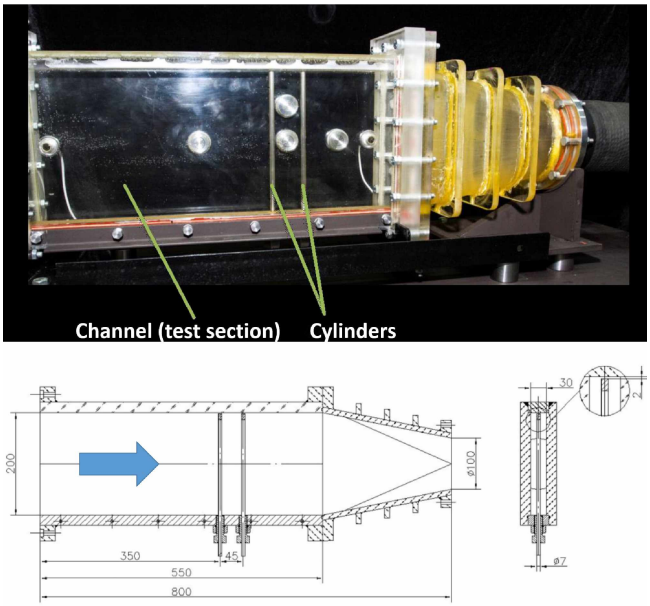

Figure 1. Picture of the test section (top) and geometrical configuration of the channel with cylinders (bottom, dimensions given in mm) of the considered experimental campaign (Bolshukhin et al (2021)).

can therefore be calculated.

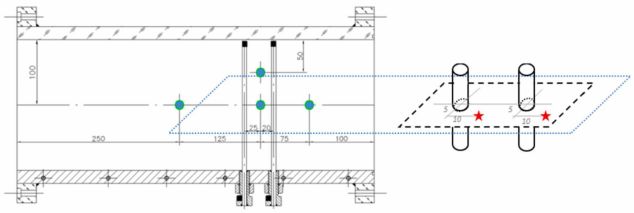

Figure 2. Locations of the measurement points (blue dots represent pressure measurements and red stars represent velocity measurements) (Bolshukhin et al (2021)).

It has to be clarify that the considered configuration is not directly representative of a NPP prototypical configuration: the cylinder diameter is smaller than typical fuel rod and tube dimensions, the spacing between the two cylinders is larger than spacing generally found in NPP components, etc. Nevertheless, the relevance of the considered experimental campaign lies in the fact that it allows to access local measurements of both fluid flow and structure vibrations: this is an innovative aspect, compared to most of the available FSI experimental results. Since beam-type structures subjected to water flow is one main configuration studied in terms of FSI issues in NPPs, the considered experimental campaign can allow a first comprehensive assessment and validation of FSI

numerical simulation approaches typically employed for NPP FSI phenomena.
Four different water flow rates were studied experimentally: the lowest one, corresponding to a free stream velocity of 0.46m/s, is considered in the present paper. This condition corresponds to a Reynolds number of about 3500, based on the cylinder diameter.

3. NUMERICAL MODEL

3.1. Fluid model

The numerical fluid domain retained is shown in Fig. 3(a). The fluid domain begins 50 mm upstream of the first cylinder, where the experimental horizontal and vertical velocity profiles are measured and can be used as boundary condition. The actual experimental mean velocity profile is imposed, whereas a flat profile of k and ω is imposed based on the hydraulic diameter of the test section and on an assumed turbulence intensity of 2%. It must be recalled that rms velocity profiles in this region are also available experimentally and should be used for future simulations.
The cross-flow through a cylinder features a given vortex shedding frequency behind it. The resulting unsteady flow features a predominant frequency corresponding to this shedding frequency. This type of unsteadiness can, theoretically, be consistently simulated by URANS approaches: these approaches are able to simulate the contribution of the coherent modes to the flow dynamics (i.e., frequencies far lower than those of the turbulent fluctuations), provided that the flow phenomena are of period larger than the time averaging period. In other words, due to their highly dissipative behavior, URANS approaches are not likely to reproduce flow instabilities, unless these instabilities are strong: vortex shedding may represent an unsteadiness strong enough to be reproduce by URANS. However, the prediction of higher shedding harmonics and of flow vortex structures is expected to be poor for URANS approaches, which can hardly reproduce the spectrum content at "high" frequencies (that is filtered and dissipated by the diffusive contribution linked to the turbulent Reynolds stress approach). For these reasons, two different CFD approaches were tested in the present study: a URANS simulation based on the $k-\omega$ SST model (Menter (1994)) and a hybrid LES/URANS simulation based on the Scale Adaptive Simulation (SAS) approach (Menter and Egorov (2010)): SAS is expected to improve the numerical results because of its LES-like behavior, in case of proper time step and mesh refinement. SAS can represent a powerful approach in terms of numerical solution improvement compared to URANS, at the same time keeping the computational cost reasonable: in fact, the SAS approach is obtained by "simply" adding a production term inside the turbulence specific dissipation (ω) transport equation, the magnitude of which is meant to increase as flow unsteadinesses increase (see Menter and Egorov (2010) for more details). Turbulent viscosity, thus, decreases allowing flow unsteadinesses to develop further. The SAS production term in the formulation developed by Menter and Egorov can be added to any ω-based turbulence model: in *code_Saturne v7* the SAS formulation was implemented inside the $k-\omega$ SST model. It has to be mentionned that the SST-SAS model of *code_Saturne* has not been formally verified and validated on reference experimental test cases, yet.

An overview of the fluid domain meshing is provided in Fig. 3(b)-(c). It is fully hexahedral, its size is around 10 million cells. Mesh convergence was checked, in terms of velocity spectra and mean velocity profiles.
Walls are expected to play a primary role in terms of fluid flow development in the considered configuration: of course, the vortex shedding is driven by the separation point along the cylinder wall, but the test section lateral walls, which are very close to the cylinders, can also influence the vortex development. For these reasons, for all walls the near wall cell center is placed at a distance y^+ lower than 1, with a growth ratio of about 1.12, in order to consistently solve the entire boundary layer region.

3.2. Solid model

The cylinder are modeled through a beam approach, based on the Euler-Bernoulli assumptions. The model was written and implemented inside *code_Saturne* by the authors.
The Euler-Bernoulli beam foundamental dynamic bending equation is:

$$\rho A \frac{\partial^2 u}{\partial t^2} + EI \frac{\partial^4 u}{\partial x^4} = F_{ext} \tag{1}$$

Where u is the displacement, ρ the material density, A the beam section, t the time, F_{ext} the external force (the fluid force), and it is assumed that the beam is homogeneous along its spanwise abscissa (x), i.e., the Young modulus (E) and the moment of inertia (I) are constant.
In order to build the finite element model (FEM) of the beam, we consider the beam element of Fig. 4, characterized by 4 degrees of freedom (DOF): the displacement of each node and the rotation of each node. The axial displacement can be decoupled from

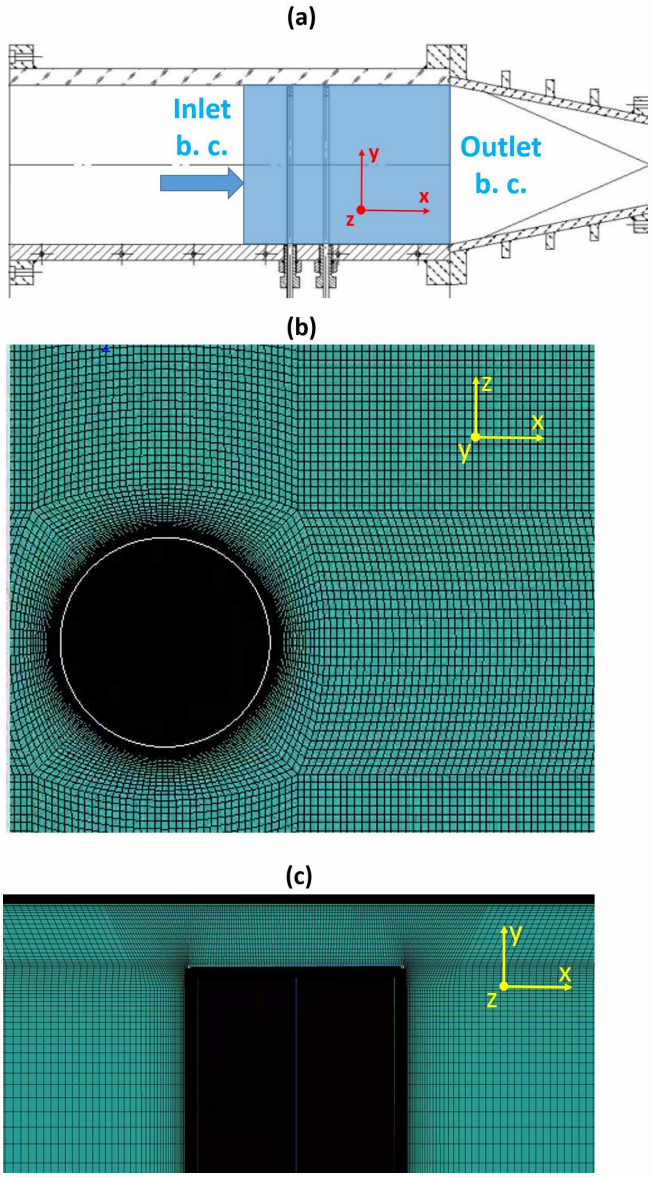

Figure 3. CFD domain: (a) region of the test section simulated, (b) meshing details along a horizontal plane and (c) meshing details in the cylinder free end region along a vertical plane.

the vertical displacement-rotation (u-ϕ) solution, and is anyway not considered in the present model, since axial stresses are neglected.

The array of the 4 nodal unknowns of the beam element is:

$$\{d\}^T = \{u_1, \phi_1, u_2, \phi_2\} \tag{2}$$

The dynamic solution of the motion of the Euler-Bernoulli beam can be obtained by the following monodimensional finite element equation:

$$[M]\{\ddot{d}_n\} + [C]\{\dot{d}_n\} + [K]\{d_n\} = \{F\} \tag{3}$$

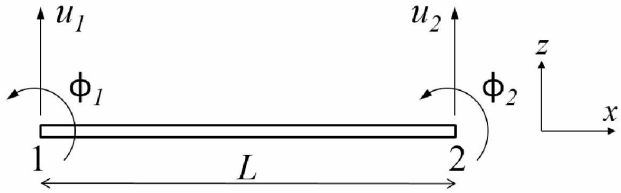

Figure 4. The 4-DOF Euler-Bernoulli beam element considered.

Where the subscript n indicates that displacements refer to the displacements of the nodes that replace the continuum solid, once the space discretization is applied. The elementary (i.e., of the beam element of Fig. 4) stiffness matrix (K_e) can be obtained by applying the principle of virtual works, considering the Hooke law from Eq. 1 and the shape functions applying to the 4 DOF beam element considered. The stiffness matrix of an Euler-Bernoulli beam is well known (see, for example, Logan (2010)) and not reported here for the sake of space.

A lumped mass matrix is retained, i.e., a diagonal mass matrix resulting from the assumption of lumping the mass of the element on its nodes. For a homogeneous Euler-Bernoulli beam, the displacement nodal masses correspond to the total mass of the element divided by 2 (two equal parts are assigned to each node); a simple and consistent assumption is to assume a zero inertial effect associated with rotational degrees (see, for example, Logan (2010)), which results in the following singular elementary lumped mass matrix:

$$[M_e] = \frac{1}{2}\rho AL \begin{bmatrix} 1 & 0 & 0 & 0 \\ 0 & 0 & 0 & 0 \\ 0 & 0 & 1 & 0 \\ 0 & 0 & 0 & 0 \end{bmatrix} \tag{4}$$

In the present model, the damping matrix is obtained simply by multiplying the stiffness matrix by a damping coefficient, representing the purely structural damping.

$\{F\}$ represents the equivalent nodal load array. Assuming an arbitrary vertical constant load applying on the element length (this assumption is consistent provided that the space discretization of the beam is fine enough to avoid significant gradients of the distributed load along the beam element), the elementary equivalent nodal load array (F_e) will be:

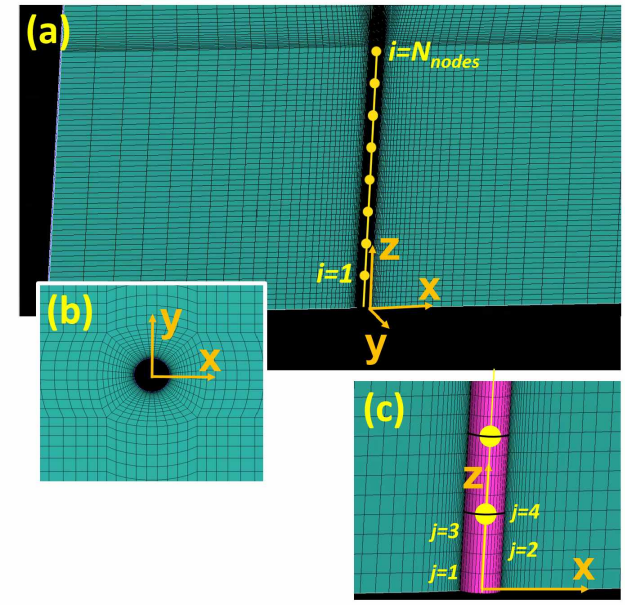

Figure 5. 3D CFD mesh and representation of the beam discretization: (a) CFD mesh cut on a x-z plane, showing the presence of the beam and its discretization into several nodes, (b) CFD mesh cut on a x-y plane, showing the presence of the beam, (c) CFD mesh faces at the fluid-solid interface (i.e., the CFD wall boundary corresponding to the cylindrical beam surface) showing the correspondance between the beam node position and the CFD mesh layer in the beam spanwise (z) direction (the hexahedral mesh is built such that all CFD nodes of a given spanwise layer are placed at the same z position).

$$\{F_e\} = p \begin{bmatrix} \frac{L}{2} \\ \frac{L^2}{12} \\ \frac{L}{2} \\ \frac{-L^2}{12} \end{bmatrix} \tag{5}$$

The elementary mass (M_e), damping (C_e) and stiffness (K_e) matrices and the elementary nodal force array (F_e) are then assembled in order to obtain the global mass (M), damping (C) and stiffness (K) matrices and the global nodal force array (F), used to solve the global beam Eq. 3.

3.2.1. FSI implementation and coupling

We refer to the 3D CFD mesh shown in Fig. 5, which shows an arbitrary cylindrical cantilever beam inside a fluid domain (z=0 in Fig. 5 represents the fixed boundary condition of the cantilever beam). The present FSI coupling approach is meant to be applied to hexahedral meshes along the beam wall, built such that all CFD nodes of a given vertical layer are placed at the same beam spanwise position (direction z in Fig. 5). Each beam element generally contains several CFD mesh faces/nodes, since the beam space discretization is generally coarser than the CFD one. In the example of Fig. 5(c), four CFD mesh layers (j) are comprised between two beam nodes. It is chosen to place all beam nodes in correspondence with the nodes of one CFD mesh layer, as presented in Fig. 5(c) (this is why only hexahedral meshes are suitable). The distance between two beam nodes (i.e. the length of the beam elements) is kept as much constant as possible along the beam (the distance depends on the actual CFD mesh distribution along the beam wall). Once the beam node positions are defined, the mass, damping and stiffness elementary and, then, global matrices can be built.

In order to build the equivalent load array, it is assumed that each node sees half the force of the upstream beam element plus half the force of the downstream beam element (except for the node placed on the free end, that receives only half the force of the upstream element).

The algorithm proposed by Hilber (1977), which represents a slight modification of the standard Newmark approach, is retained to solve Eq. 3 and calculate the time and space evolution of the beam node displacement. For a general beam moving in the two tranverse directions (drag and lift directions, in case of a cross-flow configuration), two independent (uncoupled) equations (Eq. 3) are solved, one for each direction.

The FSI simulation is based on the Arbitrary Lagrangian Eulerian approach (available in *code_Saturne*) allowing the mesh deformation in order to take into account the fluid-solid interface motion. The mesh deformation is calculated by a mesh diffusion equation, the boundary condition of which is the moving wall displacement.

The fluid forces calculated by the CFD are transferred to the beam finite element model at the end of each time step. These forces are used to calculate the beam node displacements, and the mesh deformation is imposed consistently. The updated CFD mesh configuration is used for the following time step, and so on. No inner fluid-solid sub-iterations are realized within each time step. The resulting FSI coupling approach is 2-way explicit. This type of algorithms are stable and accurate provided that the numerical time step is low enough, compared to the specific FSI mechanism. In other words, 2-way explicit approaches can provide accurate results only if the evolution of the fluid-solid configuration (for example, the evolution of the structure deformation) along one time step is small enough to be consistently

predicted by one single fluid-solid iteration.

4. RESULTS

Before discussing the results, some details about the numerical parameters retained for the present simulations are recalled.
The time-step size for the SST-SAS simulation is driven by the CFL condition: the CFL should be kept lower than at least 1 (ideally lower or equal to 0.5), in the regions where a LES-like behavior is desired. For the present simulations, a time-step equal to $1.8 \cdot 10^{-4}$s was retained (for both the SST and the SST-SAS simulations), which allowed to keep the mean CFL lower than 0.5 everywhere, except in the acceleration region around the cylinder, where the CFL could locally slightly exceed one. It has to be mentioned that a first order time discretization was retained, also for the SAS, a higher order scheme is not currently available. As mentioned in paragraph 3.1, CFD mesh convergence was checked in terms of velocity profiles and velocity spectra behind the cylinders.
Regarding the solid model, the cylinders were discretized into 30 nodes, which results in a beam finite element about 7mm long (cylinder length divided by the number of nodes). The consistency of the results provided by the solid model was checked in terms of vibration frequency and damping along a free vibration test in static air and water: the calculated results are very close to the experimental ones. No change in terms of natural frequency and damping was observed for finer discretization: the solid mesh is therefore considered converged. The nominal density of the structure needed to be slightly modified locally, in order to obtain the correct mass distribution that is affected by the presence of the accelerometers.
The physical simulated time was 20 seconds. The simulations required about 240 hours of computational time, for a parallel computation on 80 processors: therefore, 2 seconds of physical transient were calculated per 24 hours, which can be considered a relatively fast FSI simulation and prove the interest of implementing a reduced-order structure model inside a CFD code.

4.1. Flow velocity

Results are first analysed in terms of flow behavior behind the cylinders. Fig. 6 shows the PSD of the velocity behind the first cylinder. Both the SST and the SST-SAS models predict a consistent vortex shedding frequency (at about 20Hz), even if slightly underestimated. The amplitude of the experimental peak at the shedding harmonic is also consistently calculated. The PSD calculated by the SST

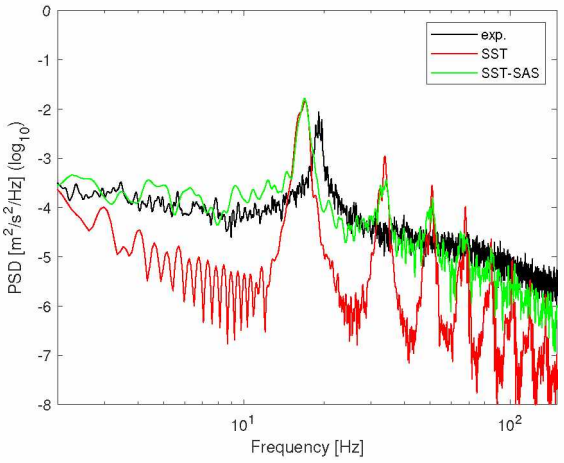

Figure 6. PSD of the velocity behind the first cylinder.

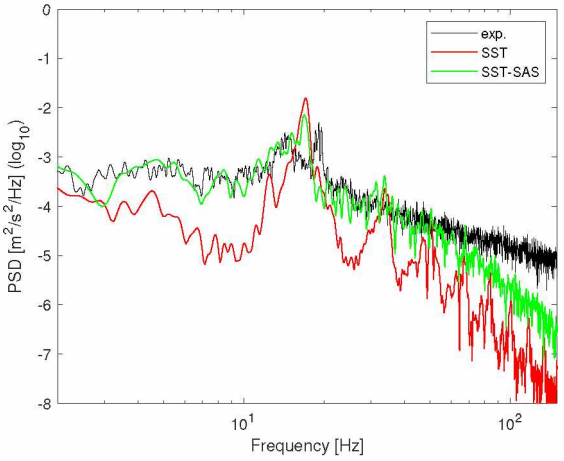

Figure 7. PSD of the velocity behind the second cylinder.

shows a cascade of harmonics, which is not present in the experimental PSD; moreover, the energy content between the different peaks is largely underestimated, compared to the experimental values. Also for the SST-SAS, some higher harmonics are present, that are not observed in the experimental PSD: these peaks are less pronounced than for the SST, and the energy content calculated by the SST-SAS is almost as high as the experimental one, up to 150Hz. A clear improvement at low frequencies (lower than the shedding harmonic) is also observed once the SAS is activated.
The PSD of the velocity behind the second cylinder is presented in Fig. 7. Also in this case, the SST underestimates significantly the content of the experimental PSD, and predicts a cascade of peaks, which

are not present in the experimental results. The spectrum obtained by the SST-SAS is much closer to the experimental one in terms of energy content, even if it decreases faster than the experimental one starting from about 70Hz. In terms of shedding frequency, the experimental PSD behind the second cylinder shows two main peaks, whereas the numerical solution only calculates one, placed in the middle of the two experimental ones.
Based on these results, there is no doubt that the activation of the SAS significantly improves the numerical results.

4.2. Cylinder vibrations

The vibration response of the cylinders is now analysed. Fig. 8 presents the PSD of the acceleration of the first cylinder. Regarding the experimental PSD, one can notice two main harmonics: the first one, at around 20Hz, corresponds to the vortex shedding harmonic, the second one, at 98Hz, corresponds to the cylinder natural frequency harmonic. The shedding harmonic is excited by the fluctuating force induced by the vortex shedding mechanism: since this is the predominant mode of the flow, the one-degree-of-freedom structure (the cylinder) is excited at the same frequency of the exciting force. The peak at the cylinder natural frequency is caused by the broad spectrum of frequencies of the fluid force (see Figs. 6 and 7), associated with the turbulent nature of the flow. Fig. 8 shows that the numerical simulations are able to calculate the acceleration harmonic at the shedding frequency: this was expected, considering the correct prediction of the velocity pulsation (see Fig. 6) at the shedding frequency. The numerical results are found to even overestimate the experimental peak.

The series of peaks in the velocity PSD calculated by the SST are found also in the acceleration PSD: each velocity peak excites an acceleration harmonic. These results are not consitent with the experimental ones, and the acceleration spectrum content calculated by the SST is orders of magnitude lower than the experimental one. The activation of the SAS allows to bring the spectrum very close to the experimental one; nevertheless, the peak at the natural frequency harmonic is still underestimated of two orders of magnitude. This suggests that the turbulent spectrum is still not enough calculated by the SAS. Both the SST and the SST-SAS calculate a main peak at about 50Hz (consistently with the same peak calculated in the velocity PSD of Fig. 6), which is not present in the experimental PSD.
Fig. 9 presents the PSD of the acceleration of the second cylinder. The acceleration harmonic at the shedding frequency is well reproduced also in this case by

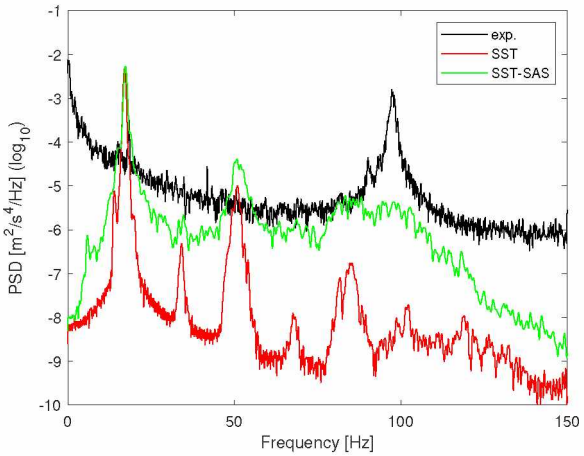

Figure 8. PSD of the vibration acceleration of the first cylinder.

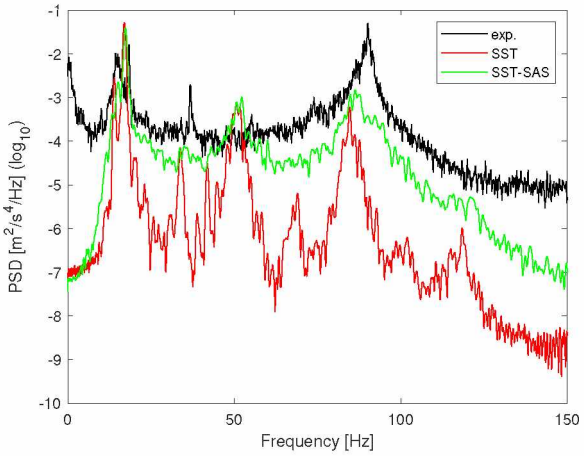

Figure 9. PSD of the vibration acceleration of the second cylinder.

both the SST and the SST-SAS. As for the first cylinder, the spectrum content of the SST is significantly lower than the experimental one, whereas the activation of the SAS allows to bring it very close to the experimental values. For the second cylinder, the acceleration harmonic at the cylinder natural frequency calculated by the SST-SAS is quite close to the experimental one (even if still underestimated by one order of magnitude).
The better numerical prediction of the acceleration PSD for the second cylinder, compared to the first one, may be due to the turbulence generated by the latter: from the numerical point of view, the second cylinder is subjected to some "resolved" turbulence (above all for the SAS), whereas the first cylinder is

subjected to the mean velocity profile imposed as inlet boundary condition (the rms velocity at the inlet is "converted" to "modeled" turbulence, i.e., the turbulent kinetic energy). This behavior is practically the same for the SST and the SST-SAS, since even for the latter the region upstream of the first cylinder has a URANS-like behavior (not enough unsteadinesses are generated in this region to trigger the SAS). Fig. 10 presents the instantaneous velocity profile and Q-criterium for the SST-SAS simulation: one can observe that, as expected, no velocity fluctuating components are present upstream of the first cylinder. An artificial generation of turbulence at the inlet may improve the numerical results for the first cylinder.
It can also be observed that the natural frequency of the second cylinder is slightly underestimated by the numerical simulation: this suggests that the added mass mechanism is modified between vibrations in static water (conditions retained to calibrate the cylinder natural frequency) and vibrations under flow rate.

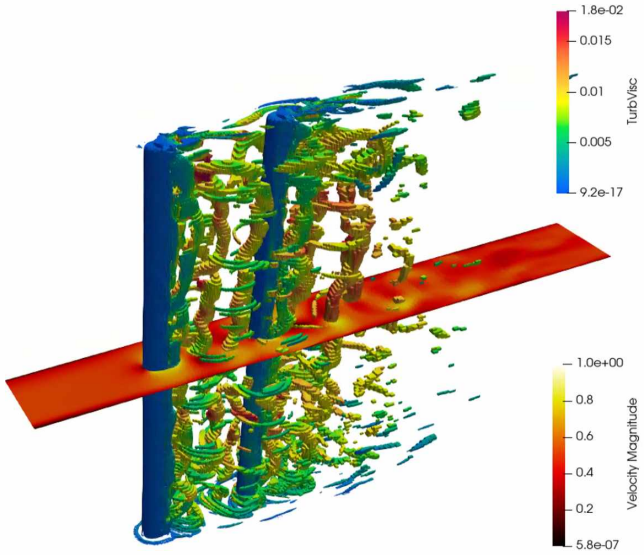

Figure 10. Q-criterium (colored by turbulent viscosity (Pa·s)) and velocity (m/s) profile along the central horizontal plane, at t=20s, for the SST-SAS simulation.

5. CONCLUSION

This paper attempts a comprehensive assessment of an FSI simulation, based on the numerical-*vs*-experimental comparison of both the fluid and the structure behaviors. The simulated configuration corresponds to an experimental campaign of two in-line cylinders subjected to water cross-flow, highly instrumented for accessing both fluid and structure details. The numerical FSI model employes CFD to model the fluid, coupled to a finite element beam model, implemented directly inside the CFD code (*code_Saturne*), to model the structure. The resulting FSI approach allows to save significant computational time in terms of FEM resolution and code-to-code data transfer, compared the general approach of coupling a CFD code to a 3D FEM code.
Numerical simulations using the SST URANS model and the SST-SAS model were performed. In terms of velocity spectra behind the cylinders, the SAS approach was found to calculate results overall consistent with the experimental ones. On the other hand, the SST model is, as expected, not able to calculate the correct content of the velocity spectrum, starting from low frequencies. Consistently with the results in terms of velocity, the vibration acceleration of the cylinders is found to be significantly underestimated by the SST, whereas the SST-SAS allows to obtain results overall close to the experimental measurements. An underestimation of the acceleration at the cylinder natural frequency harmonic is, nevertheless, observed, even for the SAS: a finer mesh and/or an artificial generation of turbulence at the inlet (aiming at providing a more consistent velocity fluctuating content) may be necessary to improve the prediction of the fluid force content.
The first main conclusion of this work is that the FSI approach developed by the authors, based on a reduced-order model for the structure directly implemented inside the open source CFD code *code_Saturne*, allows to perform FSI simulations of beam-type structures requiring relatively low computational effort and time. It can be therefore considered a promising approach for the application to larger scale industrial configurations relevant for NPPs.
The second interesting finding is that, for the cross-flow configuration considered here, the SAS approach definitely allows to calculate superior results, compared to URANS (or, at least, to URANS based on a 2-equation linear eddy viscosity model, as the one tested here). Considering that the computational time keeps unchanged compared to the standard SST (providing that the mesh and the time-step are the same), the SAS approach should be considered a powerful candidate for such flow configurations.
The simulations of experimental tests at higher water flow-rates of the here considered campaign represent a perspective for the future work.

6. REFERENCES

Liu, et al, 2017 Numerical investigations on flow-induced vibration of fuel rods with spacer grids subjected to turbulent flow. *Nuclear Engineering and Design* **325**: 68-77

De Santis, D., Kottapalli, S. and Shams, A., 2018 Numerical simulations of rod assembly vibration induced by turbulent axial flows. *Nuclear Engineering and Design* **335**: 94-105

De Santis, D. and Shams, A., 2019 Analysis of flow induced vibrations and static deformations of fuel rods considering the effects of wire spacers and working fluids. *Journal of Fluids and Structures* **84**: 440-465

Brockmeyer, L. et al, 2020 One-way coupled simulation of FIV in a 7-pin wire-wrapped fuel pin bundle. *Nuclear Engineering and Design* **356**

Mark A. Christon et al, 2016 Large-eddy simulation, fuel rod vibration and grid-to-rod fretting in pressurized water reactors. *Journal of Computational Physics* **322**: 142-161

Baraglia, F., Benguigui, W. and Denefle, R., 2021, A corotational finite element approach coupled to a discrete forcing method to solve hyperelastic deformation induced by two-phase flow. *Journal of Fluids and Structures* **107**

Papukchiev, A. 2019 Numerical analysis of reactor relevant vibrations using advanced multiphysics CFD-CSM methods. *Nuclear Engineering and Design* **350**: 21-32

Shinde, V. et al, 2014, Numerical simulation of the fluid-structure interaction in a tube array under cross flow at moderate and high Reynolds number. *Journal of Fluids and Structures* **47**: 99-113

Berland, J., Deri, E. and Adobes, A. et al, 2016, Investigation of Cross-Flow Induced Vibrations in a Normal Square Tube Array by Means of Large-Eddy Simulations for Tube Damage Risk Assessment. *Proceedings of Computational Fluid Dynamics for Nuclear Reactor Safety Applications-6 (CFD4NRS-6), 13-15 September 2016 Cambridge, United States*

Bolshukhin, M. A. et al, 2021, Dynamic measurements of the flow and structure oscillations to validate FSI calculations. *Nuclear Engineering and Desig* **381**.

Menter, F. R., 1994, Two-Equation Eddy-Viscosity Turbulence Models for Engineering Applications *AIAA Journal* **32(8)**: 1598-1605

Menter, F. R. and Egorov, Y., 2010, The Scale-Adaptive Simulation Method for Unsteady Turbulent Flow Predictions. Part 1: Theory and Model Description. *Journal of Flow, Turbulence and Combustion* **85**: 113-138

Logan, D. L., 2018, A first course in the Finite Element Method, Fourth Edition. *Springer*

Hilber, H. M. and Hughes, T. J. R. and Taylor, R.L., 1977, Improved numerical dissipation for time integration algorithms in structural dynamics. *Earthquake engineering and structural dynamics* **5**: 283-292